



Influence of thermal behavior along deposition direction on microstructure and microhardness of laser melting deposited metallic parts

Dongdong Gu^{1,2} · Lei Du^{1,2} · Donghua Dai^{1,2} · Kaijie Lin^{1,2} · Mujian Xia^{1,2} · Shuhui Li^{3,4} · Ji He^{3,4}

Received: 20 February 2019 / Accepted: 3 June 2019 / Published online: 8 June 2019
© Springer-Verlag GmbH Germany, part of Springer Nature 2019

Abstract

To have a comprehensive understanding of thermal development of a laser melting deposition (LMD) additive manufacturing process, a three-dimensional finite element model was proposed to investigate the thermal behaviors of the initial, central and terminal locations along the deposition direction of the laser-deposited tracks of Inconel 625 Ni-based alloy. The underlying influence of thermal behavior on microstructure evolution and microhardness performance in multi-track LMD-processed parts was disclosed. The simulation results showed that the heat accumulation at the initial or terminal location was more significant. The maximum cooling rate was lower and the liquid lifetime was longer at the initial or terminal location of the deposition tracks, as compared with the results produced at the central location of the track. As the dimension of the molten pool increased with the increase of the molten pool temperature, the dimension of the molten pool at the initial or terminal location was larger than that at the central location. The LMD experiments were conducted to validate the simulation. Typical dendritic columnar growth with the average primary dendrite arm spacing of 3.42 μm and 3.77 μm was observed at the initial and terminal location, respectively. In comparison, the finer columnar dendrites with the average primary dendrite arm spacing of 2.55 μm were found at the central location, due to the highest cooling rate and the shortest liquid lifetime. As a result, an enhanced microhardness (263 HV_{0.3}) was obtained at the central location, which was apparently higher than that at the initial (241 HV_{0.3}) or terminal (243 HV_{0.3}) location.

1 Introduction

Unlike conventional material machining methods, additive manufacturing (AM) technology is based on an entirely opposite philosophy of material added manufacturing. Laser melting deposition (LMD), based on powder feeding, is a promising AM technology applicable to the aerospace, automotive, and biomedical industries due to its flexibility in materials and shapes [1–3]. LMD is a process that blows powder into the molten pool formed by a moving laser beam to sequentially produce tracks and layers, producing three-dimensional parts with near full density and complex internal structures. Compared with conventional manufacturing techniques, the fine-grained phases/microstructures with novel properties can be obtained by LMD due to the rapid melting and solidification [4, 5]. In addition, LMD technology can be used to repair components which cannot be repaired by conventional techniques. Therefore, LMD technique provided a prospective potential to manufacture the high-performance parts with the advantages of time saving and cost saving. A variety of pure metals, alloys,

✉ Dongdong Gu
dongdonggu@nuaa.edu.cn

¹ College of Materials Science and Technology, Nanjing University of Aeronautics and Astronautics, Yudao Street 29, Nanjing 210016, Jiangsu Province, People's Republic of China

² Jiangsu Provincial Engineering Laboratory for Laser Additive Manufacturing of High-Performance Metallic Components, Nanjing University of Aeronautics and Astronautics, Yudao Street 29, Nanjing 210016, Jiangsu Province, People's Republic of China

³ State Key Laboratory of Mechanical System and Vibration, Shanghai Jiao Tong University, Shanghai 200240, People's Republic of China

⁴ Shanghai Key Laboratory of Digital Manufacture for Thin-walled Structures, Shanghai Jiao Tong University, Shanghai 200240, People's Republic of China

metal matrix composites (MMCs) and functionally graded materials (FGMs) have been successfully deposited with tailored microstructures and high performance by LMD [6–8]. Inconel 625 is a solid solution or/and precipitation strengthened nickel-based superalloy, which is widely used in aerospace, chemical, petrochemical and marine applications due to the rare synergy of favorable yield strength, creep strength, fatigue strength and excellent oxidation and corrosion resistance in aggressive environments [9]. Inconel 625 has the merits of maintaining its outstanding mechanical strength and corrosion resistance from moderate service temperature up to 650 °C; therefore, it is favorable for hot-end components [10, 11]. In general, the excellent high-temperature performance mainly attributes to the inherent solid-solution strengthening effect of the refractory metal elements such as niobium and molybdenum in Ni–Cr matrix. Researchers have pointed out that the solidification process of Inconel 625 is accompanied by the segregation of Nb and Mo element and as a result, Laves phase is precipitated in the interdendritic regions [12, 13]. It is well known that the microstructures are extremely sensitive to the thermal behavior and the attendant properties of the components are considerably affected by the microstructure. Therefore, it is essential to study the complex thermal behavior during LMD process and its influence on microstructure and mechanical properties. When zigzag deposition strategy is applied, diverse thermal behaviors might occur at different locations along the longitudinal direction, leading to the non-uniform microstructure and mechanical properties obtained in the LMD-processed parts. Physical phenomena related to LMD including laser–powder interaction, heat transfer, mass transport, convection flow and phase transformations are difficult to be studied through experiments [14, 15].

Numerical simulation can offer an inner view of physical phenomena in the process of LMD. To date, different three-dimensional models using the finite element method (FEM) have been proposed by many researchers to calculate temperature field, velocity field and stress field in AM process [16–19]. Some researchers simulated the volume shrinkage behavior during the laser densification process [20]. Gao et al. proposed a single-track model to study the thermal field in laser cladding process [21]. Alimardani et al. built a thin-wall multilayer structure model to study temperature field and stress field during manufacturing process and their influence on preheating and clamping the workpiece to the positioning table [22]. Manvatkar et al. developed a three-dimensional model to calculate heat transfer and fluid flow in laser-assisted multilayer AM process [23]. A three-dimensional numerical model considering the transient, heat and mass transfer in the liquid metal flow was developed by Gan et al. for the laser AM of Ni-based alloy. They focused on the microstructure evolution along the building direction and revealed that coarser solidified grains were generated in the upper layers due to the lower cooling rate

[24]. Zhang et al. indicated that the temperature increased with the increase of deposition height, resulting in the formation of lower hardness at the upper region [25]. Numerical models were also developed to investigate the microstructure evolution during LMD process [26, 27]. However, most of the previously reported works mainly focus on the processing parameters, the temperature history and the microstructure evolution in the single track or thin walls and the investigations on the variation of microstructure along the deposition direction of the same LMD deposition track are limited.

In this paper, a three-dimensional finite element model was proposed to investigate the thermal behavior of different locations along the deposition direction in LMD process. Latent heat of phase change, multiple heat transfer, and temperature-dependent thermal–physical properties were considered to obtain accurate calculated results. Quantitative data of the thermal behavior, the cooling rate and the liquid lifetime of variable monitoring points at the initial, the central and the terminal locations of the same deposition track were investigated. Thermal behavior at different locations along longitudinal direction was analyzed. LMD experiments were carried out and the microstructure and microhardness at different regions of LMD-processed Inconel 625 were investigated to validate the simulation results.

2 Finite element modeling and experiment procedures

2.1 Finite element modeling

2.1.1 Thermal analysis

The spatial and temporal distribution of temperature field conforms to the transient energy conservation equation, which can be expressed as:

$$\frac{\partial(\rho(T) \times C_p(T) \times T)}{\partial T} = \frac{\partial}{\partial x} \left(K_x(T) \times \frac{\partial T}{\partial x} \right) + \frac{\partial}{\partial y} \left(K_y(T) \times \frac{\partial T}{\partial y} \right) + \frac{\partial}{\partial z} \left(K_z(T) \times \frac{\partial T}{\partial z} \right) + \dot{Q}(x, y, z), \quad (1)$$

where $\rho(T)$ is the temperature-dependent material density, C_p is the temperature-dependent specific heat, $K_x(T)$ is the temperature-dependent thermal conductivity, and $\dot{Q}(x, y, z, t)$ is the heat generated per unit volume. In this paper, taking into account the effects of Marangoni–Rayleigh–Benard convection on heat transfer within the molten pool, thermal conductivity is enhanced by a factor ζK . The distribution of laser power intensity is assumed to be a circular Gaussian model:

$$q = \frac{2AP}{\pi R^2} \exp\left(-\frac{2r^2}{R^2}\right), \quad (2)$$

where R is the laser beam radius, r is the distance from center of the laser beam, A is the laser energy absorptivity and P is the laser power.

The latent heat occurred in the phase change, such as the transition of solid–liquid. In this paper, the enthalpy is used to define the latent heat, expressed as a function of temperature:

$$H = \int \rho C_p dT, \tag{3}$$

where H is the enthalpy, ρ is the material density of Inconel 625 (8440 kg/m³), C_p is the specific heat capacity and T is the temperature of the melt formed in LMD process.

2.1.2 Initial and boundary conditions

The initial condition of the temperature distribution in the deposition part and substrate at time $t=0$ is defined as

$$T(x, y, t)|_{t=0} = T_{amb}(x, y, z) \in D, \tag{4}$$

where D is the activated three-dimensional domain in the physical model and T_{amb} is the ambient temperature.

The convection and radiation boundary condition can be considered as

$$k\nabla T \cdot n|_s = [-h(T - T_a - \varepsilon\sigma(T^4 - T_a^4))] \Big|_s \quad \text{if } \notin \Omega, \tag{5}$$

where n is the normal vector of the surface, ε is the emissivity, h is the heat convection coefficient, σ is the Stefan Boltzmann constant, S represents the surface which is exposed to heat fluxes, radiation and convection, and Ω represents the surface that is exposed to laser beam. Furthermore, the influence of the moving laser beam can be regarded as the surface heat source in the boundary condition as follows:

$$k\nabla T \cdot n|_s = [aq - h(T - T_a) - \varepsilon\sigma(T^4 - T_a^4)] \Big|_s \quad \text{if } S \in \Omega, \tag{6}$$

where a is the absorptivity and q is the laser energy distribution on the work piece.

The incident laser beam irradiates the top surface of the work piece and a portion of laser energy is dissipated by radiation and convection. A combined heat transfer coefficient (h_1) is used to avoid the non-linear analysis and is expressed as follows:

$$h_1 = 24.1 \times 10^{-4} \varepsilon T^{1.61}, \tag{7}$$

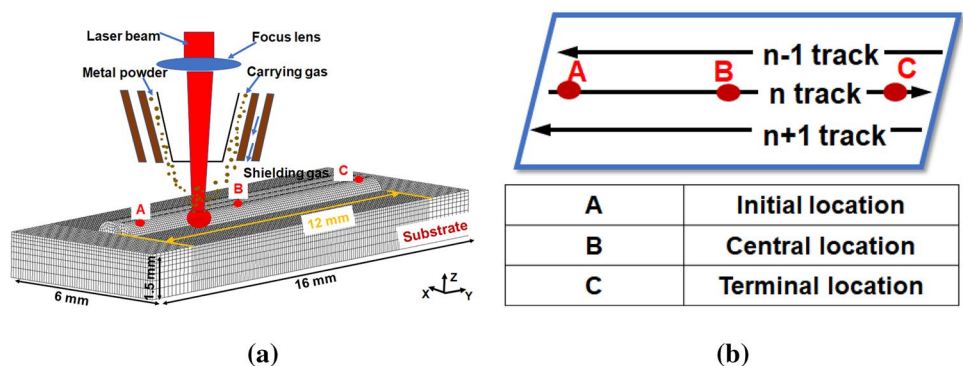
where ε is the emissivity of the substrate material and T is the solution temperature.

2.1.3 Model description

The established three-dimensional finite model and laser scan strategy during LMD process are shown in Fig. 1. In this model, the thermal conduction element SOLID70 was utilized to mesh the entire FEM. The dimensions of the FEM are shown in Fig. 1a. To achieve high calculation accuracy and reduce the computational time, a non-uniform mesh was adopted. The finer mesh was used in deposition part. For the substrate, the position near the deposition part was finely meshed, and position away from the deposition part was coarsely meshed [28]. The Zigzag deposition strategy was employed in the simulation process. For analyzing the characteristics of thermal history during LMD process, three representative points, namely Point A, Point B and Point C, located at the top surface of the initial, central and terminal locations of the n deposition track were monitored, respectively (Fig. 1b).

The optimized laser parameters were applied in the simulation: laser power (P) 800 W, scanning speed (v) 500 mm/s and powder flow rate (I) 2.4 g/min. Element birth and death technique was applied to depict the addition of metal powder in the LMD process. The killed elements were not contributing to the solution before they were activated. Before the LMD process, all elements of the deposition part were dead. With the movement of laser beam, dead elements were gradually activated, then the heat loads were applied to the laser-scanned region and finally the calculation was carried out. Moreover, heat flux boundary condition varying with time and location could be achieved by the loop statement

Fig. 1 a The established three-dimensional finite element model and schematic of LMD process; b multi-track deposition strategy and the position of monitoring point during LMD simulation process



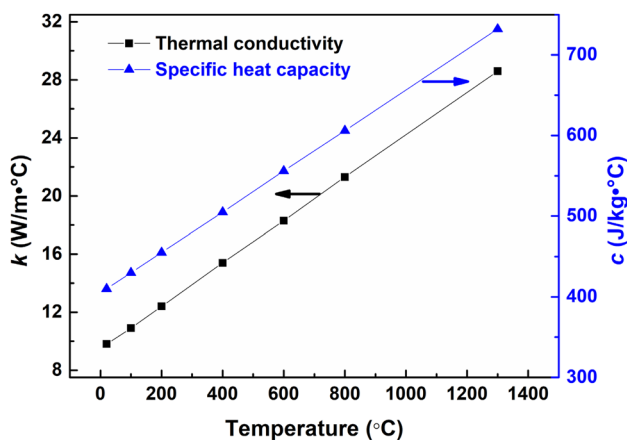


Fig. 2 Thermal conductivity and special heat capacity of Ni-based superalloy (Inconel 625) at different temperatures

APDL (ANSYS Parametric Design Language) program [29, 30]. In addition, some assumptions were made to simplify the solution process. The material in this simulation process was considered to be isotropic and homogeneous. The thermal–physical parameters of Inconel 625 were set as temperature dependent (Fig. 2) [31].

2.2 Experimental procedures

2.2.1 Powder material and LMD process

Gas-atomized Inconel 625 powder with the particle size ranging from 15 to 45 μm was used in this study. Table 1 shows the chemical contents of Inconel 625 powder. The LMD system used in this study mainly contained a Trumpf Nd:YAG laser system (Trumpf, Stuttgart, Germany) with a maximum output power of 3 kW and a focused spot diameter of 0.6 mm, a powder feeder system, a six-axis computerized

numerical control system and a coaxial powder nozzle. To validate the simulation results, identical process parameters were set as follows: laser power 800 W, scanning speed 500 mm/s, and powder feeding rate 2.4 g/min. The zigzag deposition strategy was employed in this study and the schematic of this strategy is depicted in Fig. 3a.

2.2.2 Characterization of microstructure and performance

Cross sections at different locations of LMD-processed part were observed to investigate the effect of the location variation on the microstructure evolution and microhardness by the zigzag deposition method (Fig. 3b). Three typical locations were defined: Cross sections A and C represented the initial and terminal regions of LMD-processed part (along the Y-axis), respectively. Cross section B represented the central location of LMD-processed part (along the Y-axis). The samples for metallographic examinations were prepared according to the standard procedures and etched with a mixture of HNO₃ (10 ml), HCl (15 ml) and CH₃-COOH (10 ml) for 10 s. The microstructure of sample was characterized by a GMP3 optical microscopy (Olympus Corporation, Japan) and field emission scanning electron microscopy (FE-SEM Hitachi, Japan) at an accelerating voltage of 3 kV. AHXS-1000AY microhardness tester (AMETEK, China) with a load of 0.3 kg and a dwell time of 15 s was utilized to measure the Vickers hardness.

3 Results and discussion

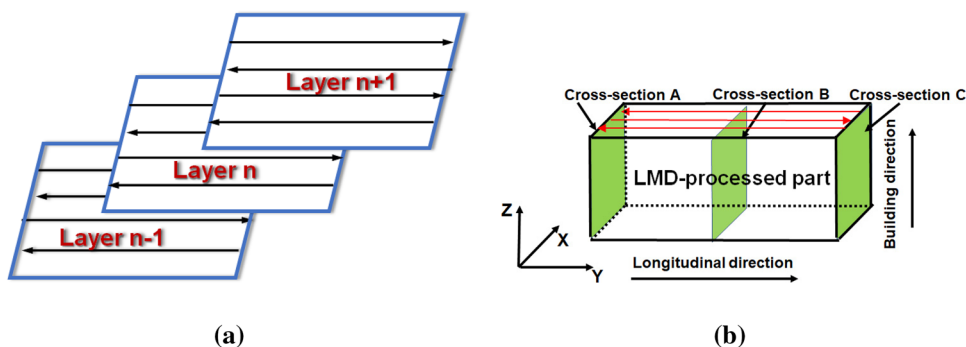
3.1 Thermal behavior

Figure 4 presents the temperature contours of the LMD-deposited tracks at different iteration time. During the LMD process, the laser energy was attenuated by the absorption

Table 1 Chemical compositions of Inconel 625 alloy powder (weight fraction, wt.%) [31]

| Ni | Cr | Mo | Nb | Fe | Co | Mn | Si | Al | Ti | C | P | S |
|---------|-------|------|-----------|----|----|-----|-----|-----|-----|-----|-------|-------|
| Balance | 20–23 | 8–10 | 3.15–4.15 | 5 | 1 | 0.5 | 0.5 | 0.4 | 0.4 | 0.1 | 0.015 | 0.013 |

Fig. 3 a Zigzag deposition method during LMD experimental process. b Schematic of different cross sections of LMD-processed part



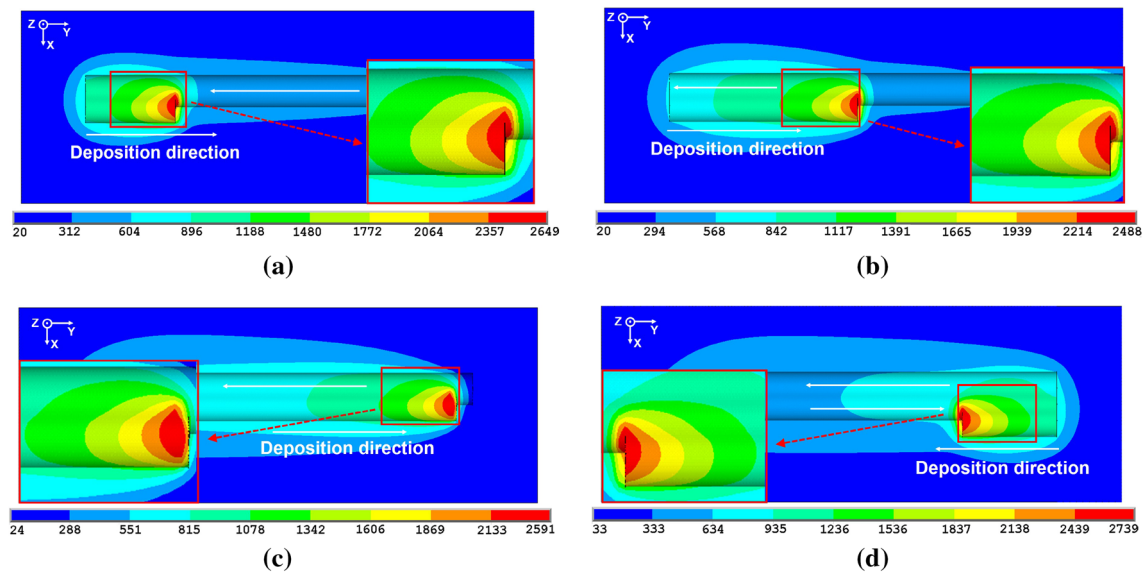


Fig. 4 Three-dimensional temperature distribution at different simulation times during LMD process: **a** $t = 0.03$ s, **b** $t = 0.036$ s, **c** $t = 0.047$ s, **d** $t = 0.054$ s

and reflection of the powder before reaching the deposition surface. The remainder laser energy was absorbed by the deposition surface, leading to the rapid heating and the resultant formation of the melt. Then, consecutive tracks and layers were additively deposited. It was obvious that the temperature distribution of multi-track deposition was no longer symmetrical to the laser beam center compared with single-track deposition, which was attributed to the heat accumulation and heat conduction between adjacent deposition tracks. In addition, it seemed that the temperature contour was skewed to the former deposition tracks (insets in Fig. 4). A large amount of the heat input was applied in a limited area, especially in front of the melting region, leading to the formation of the denser isothermal curves in the front of the molten pool (Fig. 4). Simultaneously, the temperature of the adjacent zone of the $n - 1$ and n deposition track was exceeded the liquidus temperature of Inconel 625 (1350 °C). In other words, the $n - 1$ deposition track had been partly re-melted, which was conducive to the generation of the good metallurgical bonding between adjacent tracks. As the n deposition track was processed, the maximum temperature was varying with time (Fig. 4). As the n deposition track was processed, there was a significant heat accumulation, caused by the previous $n - 1$ deposition track. Hence, higher maximum temperature (2649 °C) was observed in the previous solidified n track (Fig. 4a). With the processing of deposition, the thermal effect of the $n - 1$ deposition track on the n deposition track was gradually weakened, leading to the reduced maximum temperature at the central of the n deposition track (2488 °C). At the terminal location of the

n deposition track, the maximum temperature was slightly increased to 2591 °C due to the overall heat accumulation effect during LMD process (Fig. 4c). Besides, when the $n + 1$ track began to deposit, the maximum temperature increased further to 2739 °C (Fig. 4d).

To quantitatively analyze the thermal history of variable points at different locations of the n deposition track, temperature distribution as a function of iteration time for monitoring points A, B and C was compared. Temperature profiles versus processing time of variable monitoring points during the LMD process are depicted in Fig. 5a. The heating and cooling rates during the rapid heating/melting and cooling/solidification processes of each point could be noticed from Fig. 5a. Initially, points A, B and C were inactive and the temperature obtained in these points was equal to the room temperature (20 °C). Then, points A, B and C were activated one by one when the laser beam scanned to the corresponding location. The temperature reached the peak rapidly and then decreased fleetly with the laser beam moving away. When laser beam interacted with the initial location of the n deposition track, the maximum temperature of the molten pool was 2984 °C (point A in Fig. 5a). When the laser beam was moved to the point B, the maximum temperature was decreased to 2488 °C, near 500 °C lower than that of the point A. For the terminal region, the maximum temperature of the point C was elevated to 2591 °C. When the $n + 1$ deposition track was processed, part of the n deposition track was re-melted due to the overlapping between two adjacent tracks. As a result, it was noteworthy that the thermal history of the monitoring point C consisted of

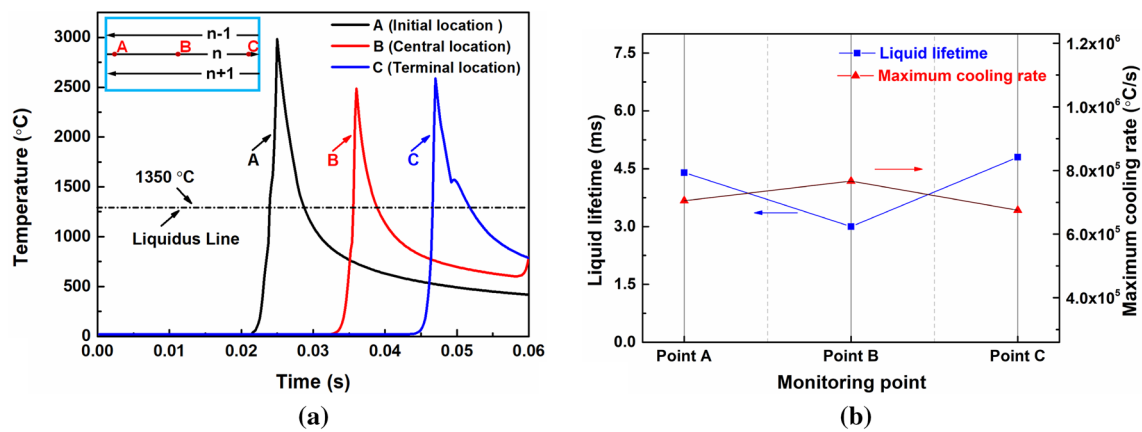


Fig. 5 **a** Temperature profiles of different monitoring points versus processing time; **b** variation of the liquid lifetime and maximum cooling rate of molten pool at monitoring points A, B and C

double-peak thermal cycles and the second peak temperature was as high as 1573 °C, exceeding the liquidus temperature of Inconel 625.

The liquid lifetime and the maximum cooling rate could also be obtained from the predicted temperature history during the LMD process. Figure 5b presents the variation of the liquid lifetime and maximum cooling rate of molten pool at points A, B and C. It was shown that the liquid lifetime along the deposition direction showed a variation from the increase to decrease, while the maximum cooling rate had an opposite variation trend (Fig. 5b). The liquid lifetime of the points A, B and C was predicted to be 4.4 ms, 3 ms and 4.8 ms, respectively. Furthermore, the maximum cooling rate of the points A, B and C was predicted to be 7.05×10^5 °C/s, 7.67×10^5 °C/s and 6.75×10^5 °C/s, respectively (Fig. 5b).

It is well known that the dimension of molten pool has a positive relationship with the temperature. The geometrical

shape and dimension of the molten pool at different locations were analyzed. The length was parallel to the longitudinal direction, the width was perpendicular to the longitudinal direction and the molten pool depth was derived from the top to the bottom of the molten pool along the Z-axis (parallel to the building direction) (Fig. 6a). Figure 6b shows the evolution of the molten pool dimensions corresponding to the different locations of the *n* deposition track based on the zigzag deposition strategy. As stated previously, the temperature at the initial or terminal location of the deposition tracks was higher and the liquid time was longer, as compared with the parameters produced at the central location. Hence, it indicated that dimensions of the molten pools at the initial and terminal location were larger than those at the central location of the deposition tracks. Three dimensions of the molten pool in the initial region of the *n* deposition track were approximately 1.68 mm (length), 1.26 mm (width) and 0.82 mm (depth), respectively

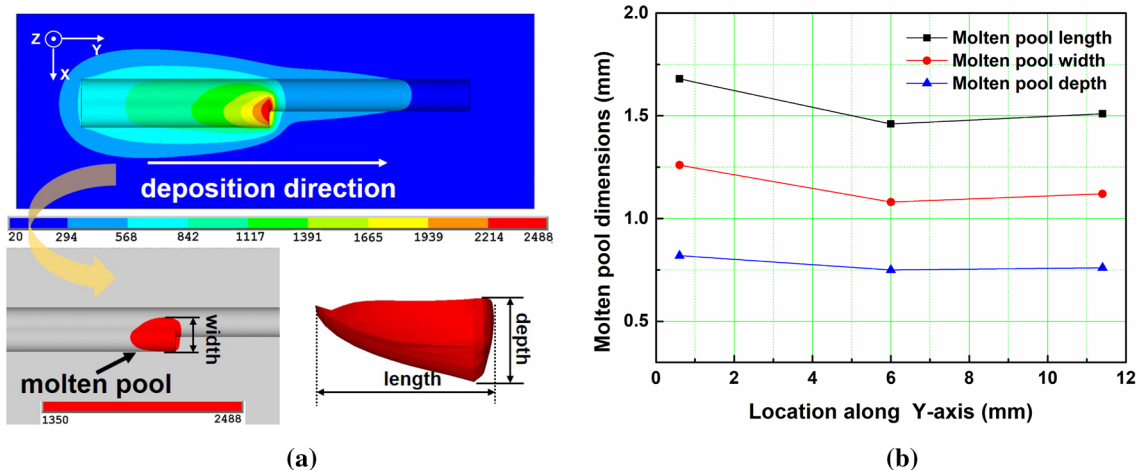


Fig. 6 **a** Schematic of molten pool dimensions; **b** evolution of the molten pool dimensions corresponding to the different locations of the *n* deposition track

(Fig. 6b). Comparing three dimensions of the molten pool at the central location with these at the initial location of the n deposition track, the length (1.46 mm), width (1.08 mm) and depth (0.75 mm) of the molten pool at the central location showed a decrease of 13.1, 14.3 and 8.5%, respectively (Fig. 6b). Moreover, three dimensions of the molten pool in the terminal region of the n deposition track were approximately 1.51 mm (length), 1.12 mm (width) and 0.76 mm (depth), respectively (Fig. 6b).

3.2 Experimental validation by microstructure

Typical metallographic microstructure OM images of the central location (cross section) and initial location (longitudinal section) of the LMD-processed Inconel 625 track are illustrated in Fig. 7. The characteristic layerwise microstructure with clear molten pool boundaries can be seen. The molten pools exhibited the arc-shaped configuration, which was ascribed to the Gaussian energy distribution of the laser beam. It was evident that no obvious defects, such as apparent pores and cracks, could be found from the cross section of central location (Fig. 7a). However, obvious crack was detected from the longitudinal section of the initial location (Fig. 7b). Cracks might be caused by two main factors. Firstly, the temperature at the initial location of the LMD-processed part was higher than that at the central location of the LMD-processed part (Fig. 5a), indicating that there was a severe heat accumulation phenomenon at the initial location of the LMD process. Meanwhile, the higher temperature gradient was generated at this location, which might lead to the formation of larger thermal stress; as a consequence, thermal cracks or deformation tended to occur to release the stresses [32] (Fig. 7b). Secondly, the dynamic viscosity μ within the molten pool could be defined by [33]

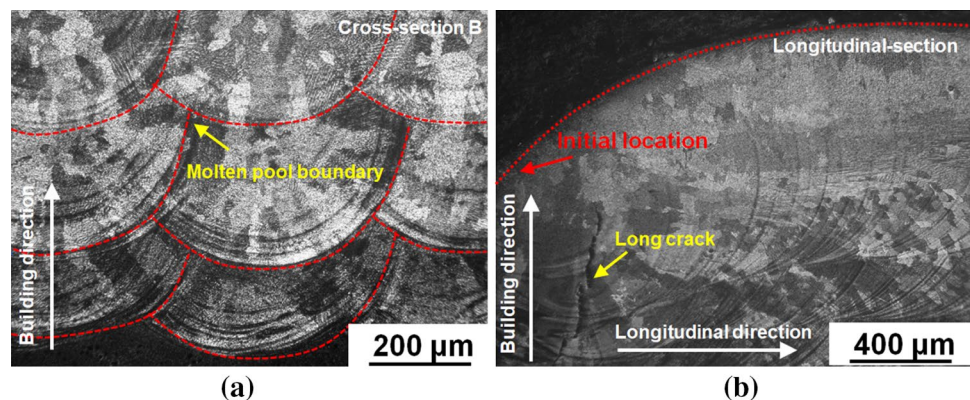
$$\mu = \frac{16}{15} \sqrt{\frac{m}{k_B T}} \gamma, \quad (8)$$

where m is the atomic mass and k_B is the Boltzmann constant. T is the temperature of the molten pool, and γ is the surface tension of the Inconel 625 liquid. Higher T resulted in a decrease in μ (Eq. 8), hence increasing the shrinkage rate during solidification process. Thus, high thermal stresses tended to generate, resulting in the formation of thermal cracks in the solidified part [34] (Fig. 7b). Besides, it could be found that the height at the initial location of the LMD-processed part was relatively low (Fig. 7b). The liquid lifetime of the molten pool at the initial location of the LMD-processed part was longer than that at the central location of the part (Fig. 5b). Therefore, a higher temperature and longer liquid lifetime of the molten pool led to a lower melt viscosity and higher capillary instability of the liquid [35], leading to the sufficient wetting in the molten pool at the initial location.

The cross-sectional FE-SEM images of LMD-processed Inconel 625 are illustrated in Fig. 8. It could be seen that the typical microstructure at the bottom of molten pool was the columnar dendritic structure. The grain growth orientation was influenced by heat flux directions as well as the preferred growth orientation related to the crystal structure [36]. It is well known that the major heat is dissipated by the thermal conduction of substrate or previously deposited layers during the LMD process [37]. Consequently, columnar dendrites parallel to the building direction were apparently observed. Typically dendritic columnar growth with average primary dendrite arm spacing of 3.42 μm was observed in the cross section A. Columnar dendrites with average primary dendrite arm spacing of 3.77 μm could be seen in the cross section C. For cross section B, relatively finer columnar dendrites with the average primary dendrite arm spacing of 2.55 μm were formed. The results indicated that coarser columnar dendrites with larger primary dendrite arm spacing tended to generate at the initial and the terminal location of LMD deposition tracks, while comparatively refined columnar dendrites with smaller primary dendrite arm spacing were formed at the central location.

Davies et al. [38] proposed a relationship between primary dendrite arm spacing and cooling rate:

Fig. 7 The cross-sectional and longitudinal-section OM images of LMD-processed Inconel 625 superalloy with laser power p of 800 W, scanning speed v of 500 mm/s: **a** cross section B (X–Z plane); **b** longitudinal section (Y–Z plane)



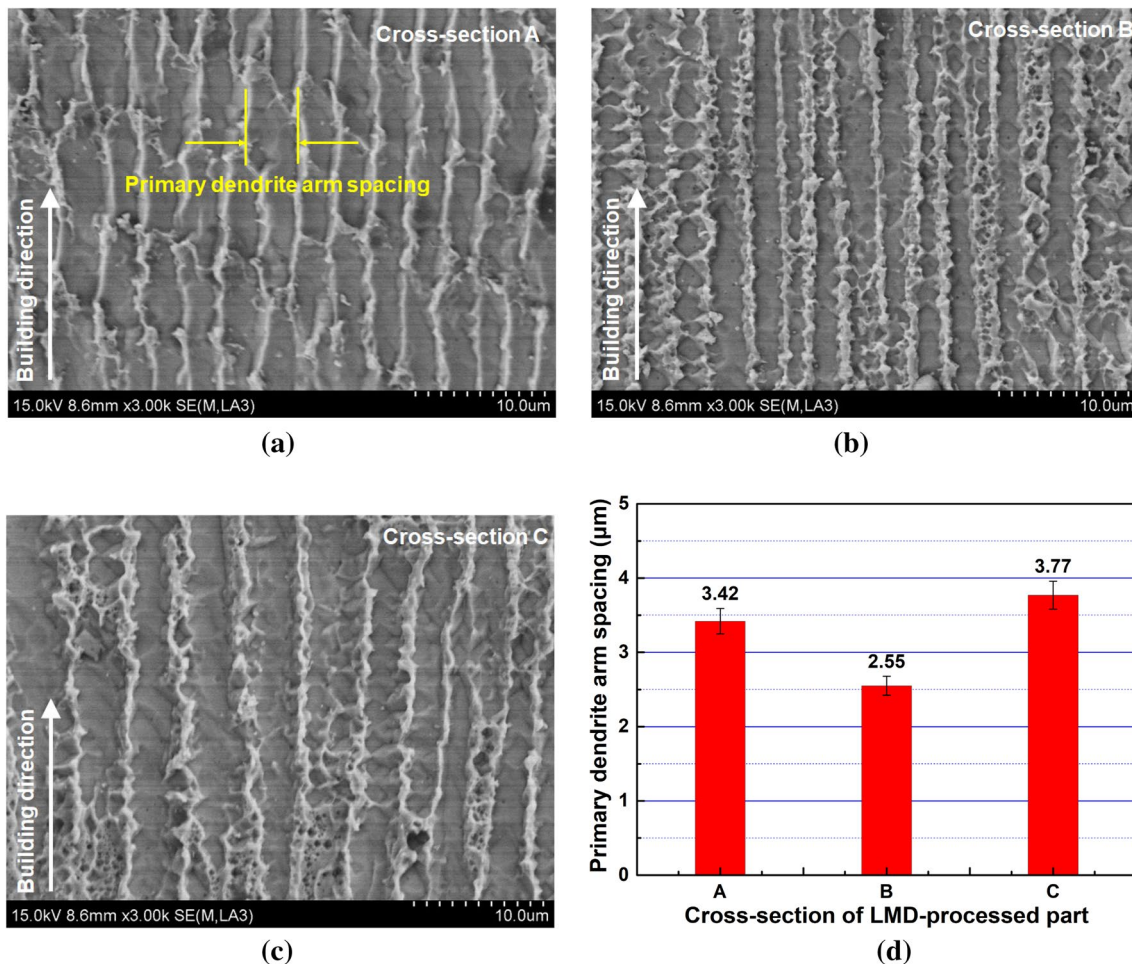


Fig. 8 FE-SEM images of different cross sections of LMD-processed Inconel 625 superalloy: **a** cross section A, **b** cross section B, **c** cross section C; **d** the average of primary dendrite arm spacing of variable cross section of LMD-processed Inconel 625 superalloy

$$\lambda_1 = 97 \pm 5 \left(\frac{\partial T}{\partial t} \right)^{0.36 \pm 0.01}, \quad (9)$$

where λ_1 is the primary dendrite arm spacing, $\frac{\partial T}{\partial t}$ is the cooling rate. It indicated that larger cooling rate could give rise to smaller primary dendrite arm spacing, improving the diffusion of solute, which was beneficial to enhance the mechanical properties of the LMD-processed part. The simulation results showed that the maximum cooling rate at the initial location and terminal location of the deposition tracks was lower than that at the central location. Besides, longer liquid time at the edge of the LMD-processed part provided adequate time for grain growth. As a result, lower cooling rate and longer liquid time contributed to the formation of coarser columnar dendrites with larger primary dendrite arm spacing at the initial and the terminal location of the LMD-processed part.

3.3 Experimental validation by microhardness performance

To investigate the mechanical properties at different regions of the LMD-processed Inconel 625 part, the microhardness test was conducted. Figure 9 presents the microhardness distribution and the average microhardness of variable cross section of LMD-processed Inconel 625. The microhardness of the cross section A varied in a range from 232 to 248 HV_{0.3} and the average value was 241 HV_{0.3}. Meanwhile, for the cross section C, the microhardness was in the range of 236–249 HV_{0.3} with apparent fluctuation and the mean microhardness was 243 HV_{0.3}. Interestingly, the microhardness of the cross section B was much higher than that of the cross section A and cross section C. The microhardness of the cross section B varied in a range from 256 to 268 HV_{0.3}, and the average hardness was 263 HV_{0.3}. The

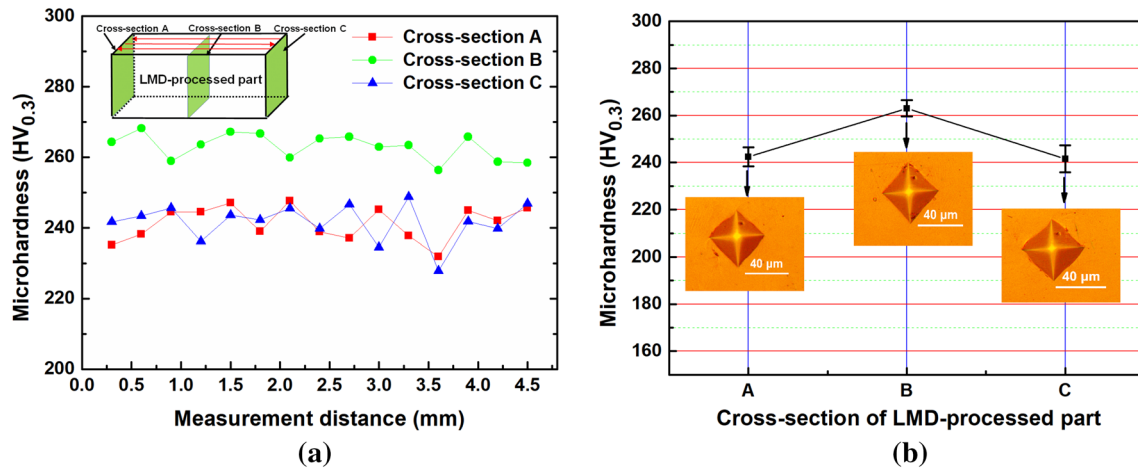


Fig. 9 **a** The microhardness profiles of different cross sections; **b** the average microhardness of different cross sections of LMD-processed Inconel 625 superalloy and the corresponding OM images of indentations

heterogeneous microhardness value was ascribed to the heterogeneous microstructure within the LMD-processed part (along the longitudinal direction). The considerably refined grain and the resultant increased density of grain boundary at the central location (Fig. 8b) contributed to the higher microhardness.

4 Conclusions

In the present study, thermal behavior during the LMD processing of Inconel 625 was researched based on FEM model. The effect of location on thermal behavior, microstructure and microhardness was analyzed by simulation and LMD experiments. The following conclusions can be drawn.

- (1) The FEM results revealed that heat accumulation effect was more significant at the initial and the terminal location of the deposition tracks. Along the longitudinal direction, the initial location exhibited the highest maximum temperature (2984 °C), followed by the terminal location (2591 °C), and the central location exhibited the lowest maximum temperature (2488 °C). The maximum cooling rate was lower and the liquid time was longer at the initial or terminal location of the deposition tracks, as compared with the parameters produced at the central location.
- (2) The dimension of molten pool, obtained by FEM, varied at different location along the longitudinal direction. The initial location had the largest molten pool dimensions (length 1.68 mm, width 1.26 mm and depth 0.82 mm), followed by the terminal location (length 1.51 mm, width 1.12 mm and depth 0.76 mm), and the central location had the smallest molten pool dimensions (length 1.46 mm, width 1.08 mm and depth 0.75 mm).

- (3) The layer-wise microstructure characteristics of the cross section with apparent molten pool outline curve could be observed, which was ascribed to the Gaussian energy distribution of the laser beam. Long cracks were generated at the initial location of the LMD-processed Inconel 625 part, which was mainly attributed to the high-temperature gradient and high shrinkage rate at the initial location. In addition, the height at the initial location of the part was lower than that at the central location due to the sufficient wetting behavior.
- (4) Various microstructures were observed at different locations along the longitudinal direction. Refined columnar dendrites with smallest primary dendrite arm spacing were formed at the central location due to the highest cooling rate and shortest liquid lifetime. The refined grain and the increased density of grain boundary at the central location contributed to the enhanced microhardness (263 HV_{0.2}) that was higher than that at the initial location (241 HV_{0.3}) or the terminal location (243 HV_{0.3}).

Acknowledgements We are grateful for the financial support from the National Natural Science Foundation of China (Nos. 51790175, 51575267); the Key Research and Development Program of Jiangsu Provincial Department of Science and Technology of China (No. BE2016181).

References

1. B. Song, Z.W. Wang, Q. Yan, Y.J. Zhang, J.L. Zhang, C. Cai, Q.S. Wei, Y.S. Shi, Integral method of preparation and fabrication of metal matrix composite: selective laser melting of in situ nano/submicro-sized carbides reinforced iron matrix composites. *Mater. Sci. Eng. A* **707**, 478–487 (2017)
2. L.W. Cheng, C.W. Cheng, K.C. Chung, T.Y. Kam, Sound absorption of metallic sound absorbers fabricated via the selective laser melting process. *Appl. Phys. A* **123**, 37 (2017)
3. R.D. Li, M.B. Wang, T.C. Yuan, B. Song, C. Chen, K.C. Zhou, P. Cao, Selective laser melting of a novel Sc and Zr modified Al–6.2 Mg alloy: Processing, microstructure and properties. *Powder Technol.* **319**, 117–128 (2017)
4. M. Navasery, S.A. Halim, A. Dehhangi, G. Bahmanrokh, M. Erfani, K.Y. Pan, S.C. Chang, S.K. Chen, K.P. Lim, M.M. Awang Kechik, Electrical properties and conduction mechanisms in $\text{La}_{2/3}\text{Ca}_{1/3}\text{MnO}_3$ thin films prepared by pulsed laser deposition on different substrates. *Appl. Phys. A* **114**, 1661–1668 (2014)
5. J.M. Wilson, Y.C. Shi, Microstructure and wear properties of laserdeposited functionally graded Inconel 690 reinforced with TiC. *Surf. Coat Technol.* **207**, 517–522 (2012)
6. T.E. Abioye, P.K. Farayibi, P. Kinnel, A.T. Clare, Functionally graded Ni–Ti microstructures synthesised in process by direct laser metal deposition. *Int. J. Adv. Manuf. Technol.* **79**, 843–850 (2015)
7. Y.J. Zhang, J.L. Zhang, Q. Yan, L. Zhang, M. Wang, B. Song, Y.S. Shi, Amorphous alloy strengthened stainless steel manufactured by selective laser melting: enhanced strength and improved corrosion resistance. *Scr. Mater.* **148**, 20–23 (2018)
8. J. Ding, P. Colegrove, J. Mehnert, S. Ganguly, P.M. Sequeira Almeida, F. Wang, S. Williams, Thermo-mechanical analysis of wire and arc additive layer manufacturing process on large multi-layer parts. *Comput. Mater. Sci.* **50**, 3315–3322 (2011)
9. G.P. Dindaa, A.K. Dasgupta, J. Mazumder, Laser aided direct metal deposition of Inconel 625 superalloy: microstructural evolution and thermal stability. *Mat. Sci. Eng. A* **509**, 98–104 (2009)
10. V. Shankar, K.B.S. Rao, S.L. Mannan, Microstructure and mechanical properties of Inconel 625 superalloy. *J. Nucl. Mater.* **288**, 222–232 (2001)
11. M. Rombouts, G. Maes, M. Mertens, Laser metal deposition of Inconel 625: microstructure and mechanical properties. *J. Laser Appl.* **24**, 2575–2581 (2012)
12. J.F. Wang, Q.J. Sun, H. Wang, J.P. Liu, J.C. Feng, Effect of location on microstructure and mechanical properties of additive layer manufactured Inconel 625 using gas tungsten arc welding. *Mat. Sci. Eng. A* **676**, 395–405 (2016)
13. H.L. Wei, J. Mazumder, T. Debroy, Evolution of solidification texture during additive manufacturing. *Sci. Rep.* **5**, 16446 (2015)
14. B. Norhafzan, S.N. Aqida, E. Chikarakara, D. Brabazon, Surface modification of AISI H13 tool steel by laser cladding with NiTi powder. *Appl. Phys. A* **122**, 384 (2016)
15. D.V. Bedenko, O.B. Kovalev, I. Smurov, A.V. Zaitsev, Numerical simulation of transport phenomena, formation of the bead and thermal behavior in application to industrial DMD technology. *Int. J. Heat Mass Transfer.* **95**, 902–912 (2016)
16. S.Y. Wen, Y.C. Shin, Modeling of transport phenomena during the coaxial laser direct deposition process. *J. Appl. Phys.* **108**, 044908 (2010)
17. T. Mukherjee, W. Zhang, T. DebRoy, An improved prediction of residual stresses and distortion in additive. *Manuf. Comput. Mater. Sci.* **26**, 360–372 (2017)
18. M.J. Xia, D.D. Gu, G.Q. Guan, D.H. Dai, H.Y. Chen, Q.M. Shi, Porosity evolution and its thermodynamic mechanism of randomly packed powder-bed during selective laser melting of Inconel 718 alloy. *Int. J. Mach. Tools Manuf* **116**, 96–106 (2017)
19. X. He, J. Mazumder, Transport phenomena during direct metal deposition. *J. Appl. Phys.* **101**, 053113 (2007)
20. K. Dai, L. Shaw, Finite element analysis of the effect of volume shrinkage during laser densification. *Acta Mater.* **53**, 4743–4754 (2005)
21. W.Y. Gao, S.S. Zhao, Y.B. Wang, Z.Y. Zhang, F.L. Liu, X.C. Lin, Numerical simulation of thermal field and Fe-based coating doped Ti. *Int. J. Heat Mass Transf.* **92**, 83–90 (2016)
22. M. Alimardani, E. Toyserkani, J.P. Huissoon, A 3D dynamic numerical approach for temperature and thermal stress distributions in multilayer laser solid freeform fabrication process. *Opt. Lasers Eng.* **45**, 1115–1130 (2007)
23. V. Manvatkar, T. DebRoy, Heat transfer and material flow during laser assisted multi-layer additive manufacturing. *J. Appl. Phys.* **116**, 124905 (2014)
24. G.Z.T. Gan, H. Liu, S.X. Li, X.L. He, G. Yu, Modeling of thermal behavior and mass transport in multi-layer laser additive manufacturing of Ni-based alloy on cast iron. *Int. J. Heat Mass Transf.* **111**, 709–722 (2017)
25. Y.J. Tang, Y.Z. Zhang, Y.T. Liu, Numerical and experimental investigation of laser additive manufactured Ti2AlNb-based alloy. *J. Alloy. Compd.* **727**, 196–204 (2017)
26. J. Song, Y.X. Chew, G.J. Bi, X.L. Yao, B.C. Zhang, J.M. Bai, S.K. Moon, Numerical and experimental study of laser aided additive manufacturing for melt-pool profile and grain orientation analysis. *Mater. Des.* **137**, 286–297 (2018)
27. S. Ghosh, N. Ofori-Opoku, J.E. Guyer, Simulation and analysis of γ -Ni cellular growth during laser powder deposition of Ni-based superalloys. *Comput. Mater. Sci.* **144**, 256–264 (2018)
28. L. Wang, S.D. Felicelli, P. Pratt, Residual stresses in LENS-deposited AISI 410 stainless steel plates. *Mater. Sci. Eng., A* **496**, 234–241 (2008)
29. A.P. Mackwood, R.C. Crafer, Thermal modelling of laser welding and related processes: a literature review. *Opt. Laser Technol.* **37**, 99–115 (2005)
30. R.B. Patil, Y. Vinod, Finite element analysis of temperature distribution in single metallic powder layer during metal laser sintering. *Opt. Laser Eng.* **47**, 1069–1080 (2007)
31. S.N. Cao, D.D. Gu, Q.M. Shi, Relation of microstructure, microhardness and underlying thermodynamics in molten pools of laser melting deposition processed TiC/Inconel 625 composites. *J. Alloy. Compd.* **692**, 758–769 (2017)
32. D.H. Dai, D.D. Gu, Thermal behavior and densification mechanism during selective laser melting of copper matrix composites: simulation and experiments. *Mater. Des.* **55**, 482–491 (2014)
33. D.D. Gu, Y.C. Hagedorn, W. Meiners, K. Wissenbach, K. Poprawe, Selective laser melting of in situ TiC/Ti5Si3 composites with novel reinforcement architecture and elevated performance. *Surf. Coat. Technol.* **205**, 3285–3292 (2011)
34. S. Das, Physical aspects of process control in selective laser sintering of metals. *Adv. Eng. Mater.* **5**, 701–711 (2003)
35. A. Simchi, H. Pohl, Effects of laser sintering processing parameters on the microstructure and densification of iron powder. *Mater. Sci. Eng., A* **359**, 119–128 (2003)
36. M. Rappaz, Development of microstructures in Fe–15Ni–15Cr single crystal electron beam welds. *Metall. Trans. A* **20**, 1125–1138 (1989)
37. X. Lin, T.M. Yue, Phase formation and microstructure evolution in laser rapid forming of graded SS316L/Rene88DT alloy. *Mat. Sci. Eng. A* **402**, 294–306 (2005)
38. N.J. Harrison, I. Todd, K. Mumtaz, Reduction of micro-cracking in nickel superalloys processed by selective laser melting: a fundamental alloy design approach. *Acta Mater.* **94**, 59–68 (2015)

Publisher's Note Springer Nature remains neutral with regard to jurisdictional claims in published maps and institutional affiliations.